scientific reports

Check for updates

OPEN

Numerical study of the performance of a three-phase horizontal separator under varying water outlet pressures

Hong-Cheol Shin, Inju Hwang, Hee-La Jang & Hyeonseok Seo✉

Horizontal gravity separators are important components in the production of unconventional petroleum resources. While tremendous efforts have made on the sizing of separators, relatively few studies have addressed their operational performance under varying outlet conditions. This study aims to investigate the effect of water outlet pressure on the performance of the separator to establish guidelines for its proper operation. Three-dimensional computational fluid dynamics (CFD) simulations are conducted using the Eulerian multiphase model and interfacial concentration area. Four water outlet pressures ranging from 7537.2 to 7421.9 Pa are examined under fixed inlet flow rates. The numerical method is validated by comparing it with experimental results. The numerical results confirm that the separation efficiency improves as the water outlet pressure decreases primarily due to the increased thickness of the oil pad. Notably, the analysis reveals that meeting residence time criteria alone does not guarantee high separation performance, as outlet pressure significantly affects fluid distribution and phase separation. These findings suggest that maintaining the water outlet pressure below 7448.5 Pa is essential for achieving efficient separation in practical operations.

List of symbols

C_D	Drag coefficient
C_{lift}	Lift coefficient
d_h	Long axis of deformable dispersed phase
d_p	Diameter of dispersed phase
Eo	Eötvös number
Eo'	Modified Eötvös number
$\vec{f}$	Drag function
$\vec{F}$	External body force
$\vec{F}_{lift}$	Lift force
$\vec{g}$	Gravitational acceleration
G	Production of turbulent kinetic energy
$h_{water,pred}$	Water height predicted by Eq. (32)
H_{weir}	Weir height
k	Turbulent kinetic energy
K	Interphase momentum exchange coefficient
L_t	Length scale of turbulent eddies
p	Pressure
Q	Flow rate
$\underline{Re}$	Reynolds number
$\overline{U}$	Phase-weighted velocity
V	Volume

Greek symbols

α	Volume fraction

Department of Environmental Research, Korea Institute of Civil Engineering and Building Technology, 283, Goyang-Daero, Ilsanseo-Gu, Goyang-Si 10223, Gyeonggi-Do, Republic of Korea. ✉email: bbashya_hsseo@kict.re.kr

γ	Specific gravity
ε	Dissipation rate of turbulence kinetic energy
η	Ratio between characteristic times
θ	Angle between two vectors
λ	Bulk viscosity
μ	Viscosity; shear viscosity
μ_t	Turbulent viscosity
ρ	Density
ρ_o	Oil density
ρ_w	Water density
$\overline{\overline{\tau}}$	Stress–strain tensor
τ_p	Particulate relaxation time
χ	Interfacial area concentration

Unconventional petroleum resources include unconventional oil (e.g., tight oil, oil shale, and bitumen) and unconventional gas (e.g., shale gas and tight gas). The estimated resources of unconventional oil and gas are expected to exceed those of conventional oil and gas sources[1]. Unconventional petroleum resources face the challenge of securing marketability as they require unconventional extraction methods such as thermal processes to reduce viscosity and hydraulic fracturing to improve reservoir permeability. However, with advances in the relevant technologies, the rising cost of conventional petroleum resources, and increasing concerns about energy security, unconventional petroleum is gradually becoming more marketable[2]. Furthermore, as global energy consumption increases, so does the demand for unconventional petroleum resources. Nonetheless, due to the relatively short period of time available for the development of extraction technologies, further research into highly efficient extraction is essential.

In the upstream part of the oil fields, separators are facilities where the fluid extracted from wells arrives first and are essential for high productivity. These separators process the extracted fluid and play a critical role in providing the fluid in a suitable form for downstream production processes by separating gas, water, and oil[3].

A horizontal gravity separator is a common type of separator. It utilizes the density differences between the phases in the mixture to facilitate phase separation. There are four flow regimes within the separators: inlet diverter, gravity settling, mist extraction, and liquid collection sections. The inlet diverter changes the direction and momentum of the inflow. The primary separation occurs between the gas and liquid phases. The gravity settling section follows the inlet diverter section. In this section, the flow velocity is reduced. The separation between the phases also progresses. The liquid droplets entrained by the gas flow fall to the gas–liquid interface, and the bubbles in the liquid phase rise and merge into the main gas flow. The thickness of the emulsion layers of the water and oil phases decreased as the fluid flowed to the outlets. The mist extraction section is located at the gas outlet. The mist extractor is installed to remove small liquid droplets that are not separated in the gravity settling section. The liquid collection section collects both the liquid and water phases and provides a retention time (or residence time) for separation.

Considerable efforts have been made to investigate the phenomena inside and the performance of the separators. To determine the size of the separators, Monnery and Svrcek[4], Bothamley and Camplbell[5–7], and Stewart and Arnold[8] have published theoretical studies based on droplet separation calculations. Experimental studies have also been conducted, for example, by Ahmed et al.[9,10] and Pun et al.[11,12]. However, owing to the complex interactions between the different phases and experimental restrictions, numerical simulations have been often used. Ahmed et al.[9] conducted numerical and experimental studies by using two pilot-scale separators. Each separator had a bucket for the water phase, a weir, and a vertical downward inlet with a horizontal plate-type diverter. The other separator had a horizontal inlet with a vertical plate-type diverter and weir. They tested the validity of two representative numerical methods: volume-of-fluid and Eulerian methods. Carvalho et al.[13,14] investigated the influence of the physical properties of the oil and inlet flow conditions on the separation performance. The separators had a horizontal inlet and a vertical plate-type diverter. They varied either the density and viscosity of the oil from 813.5 to 870 kg/m3 and 21 to 50 mPa s, respectively, or the input speed from 13 to 17 m/s. The phenomena over time were discussed focusing on the oil fraction at the oil outlet. Baghi and Karimi[15] numerically investigated the effect of an inlet diverter on the mean residence time by using the volume-of-fluid method. The four inlet diverters investigated included three plate-type diverters with bending angles of 105°, 120°, and 135°, and a spherical diverter. They discussed that the mean residence time was greatest for the plate-type diverter with an angle of 105°, which was due to the collision with the diverter.

While several previous studies have examined to size the separator properly and figure out the influences of inlet flow conditions and internal geometries on separation performance using experimental or numerical approaches, little attention has been paid to the role of outlet boundary conditions. Particularly, the impact of water outlet pressure on the internal flow field, oil pad development, and separation efficiency remains largely unexplored. Maintaining the performance of horizontal gravity separators requires proper management of both the gas–liquid interface and the oil–water interface within the separators, which are determined by the balance between the flow rates entering and exiting the separator. If a fluctuation in either the flow rate or pressure of the produced fluid occurs due to the instability of petroleum reservoir, the production system adjusts the outlet flow rates of the separators using pumps or compressors connected downstream of the separator. To compensate for unexpected fluctuations in the flow rate or pressure of the produced fluid and maintain stable separation, it is therefore crucial to investigate the effects of the outlet conditions on the performance of the separator.

The main objective of this study is to investigate the influence of the outlet pressure at the water outlet on the performance of the separator. Three-dimensional computational fluid dynamics simulations are performed to model the flow within a horizontal separator equipped with an inlet diverter and a weir. The numerical method

is validated by comparing the numerical results with experimental data. The local pressure at the water outlet is varied from 7537.2 to 7421.9 Pa. The performance of the separator is analyzed for different outlet pressures in terms of phase distributions and oil pad properties.

Numerical methods

Governing equations

ANSYS Fluent 2023, a commercial software package, is used to perform three-dimensional numerical simulations. In this study, Eulerian multiphase model is used as a multi-phase model because an emulsion layer exists during separation. This model allows for interpenetration between different phases by specifying continuous and dispersed fluids. In contrast, the volume-of-fluid model, which is another multiphase model, assumes a relatively sharp interface and therefore does not allow interpenetration between different phases. Assuming no mass transfer between the different phases and a steady state, the governing equations for the conservation of mass and momentum are as follows[16]:

$$\frac{1}{\rho_{r,q}}\left[\nabla \bullet (\alpha_q \rho_q \overrightarrow{v}_q)\right] = 0 \tag{1}$$

And

$$\nabla \bullet (\alpha_q \rho_q \overrightarrow{v}_q \overrightarrow{v}_q) = -\alpha_q \nabla p + \nabla \bullet \overline{\overline{\tau_q}} + \alpha_q \rho_q \overrightarrow{g} + \sum_{p=1}^{n}\left[K_{pq}\left(\overrightarrow{v}_p - \overrightarrow{v}_q\right)\right] + \overrightarrow{F}_q + \overrightarrow{F}_{lift,q} \tag{2}$$

where α_q, ρ_q, $\overrightarrow{v}_q$, and $\rho_{r,q}$ denote the volume fraction, density, velocity, and the volume averaged density of the q-th phase, respectively. $\overrightarrow{g}$ and p are the gravitational acceleration and pressure, respectively. The sum of the volume fractions of all phases was equal to unity. $\overline{\overline{\tau}}_q$ is the stress–strain tensor for the q-th phase and is given by,

$$\overline{\overline{\tau}}_q = \alpha_q \mu_q \left(\nabla \overrightarrow{v}_q + \nabla \overrightarrow{v}_q^T\right) + \alpha_q(\lambda_q - \frac{2}{3}\mu_q)\nabla \bullet \overrightarrow{v}_q \overline{\overline{I}} \tag{3}$$

where μ_q and λ_q denote the shear and bulk viscosity of the q-th phase. K_{pq} is the interphase momentum exchange coefficient between the q-th continuous phase and the p-th dispersed phase and is defined as

$$K_{pq} = \frac{\alpha_q \alpha_p \rho_p f}{\tau_p}. \tag{4}$$

Here, τ_p and f are the particulate relaxation time and the drag function, respectively. τ_p is obtained by

$$\tau_p = \frac{\rho_p d_p^2}{18\mu_p} \tag{5}$$

where d_p is the diameter of the bubbles or droplets in the p-th dispersed phase. The drag coefficient varies depending on the selected model. In this study, the Tomiyama model[17] is used, which defines the drag coefficient as follows:

$$f = \frac{C_D Re}{24} \tag{6}$$

where C_D is the drag coefficient. It is calculated as follows:

$$C_D = \max\left(\min\left(\frac{24}{Re}\left(1 + 0.15Re^{0.687}\right), \frac{72}{Re}\right), \frac{8}{3}\frac{Eo}{Eo+4}\right) \tag{7}$$

Here, Re and Eo are the relative Reynolds and Eötvös numbers, which are defined as follows:

$$Re = \frac{\rho_q|\overrightarrow{v}_p - \overrightarrow{v}_q|d_p}{\mu_q} \tag{8}$$

And

$$Eo = \frac{g(\rho_q - \rho_p)d_p^2}{\sigma}. \tag{9}$$

$\overrightarrow{F}_q$ and $\overrightarrow{F}_{lift,q}$ are the external body and lift forces, respectively. $\overrightarrow{F}_{lift,q}$ is the force exerted on the dispersed p-th phase due to the velocity gradient of the continuous q-th phase. It is calculated from

$$\overrightarrow{F}_{lift,q} = -C_{lift}\rho_q \alpha_p(\overrightarrow{v}_q - \overrightarrow{v}_p) \times (\nabla \times \overrightarrow{v}_q) \tag{10}$$

where C_{lift} denotes the lift coefficient. In this study, the Tomiyama lift force model[18,19] is used, which defines C_{lift} as follows:

for $Eo' \leq 4$,

$$C_{lift} = \min \left[0.288 \tanh \left(0.121 \mathrm{Re}_p \right), f \left(Eo' \right) \right] \quad (11)$$

for $4 < Eo' \leq 10$,

$$C_{lift} = f \left(Eo' \right) \quad (12)$$

and for $Eo' > 4$,

$$C_{lift} = -0.27 \quad (13)$$

where,

$$f \left(Eo' \right) = 0.00105 Eo'^3 - 0.0159 Eo'^2 - 0.0204 Eo' + 0.474 \quad (14)$$

Here, Eo' is a modified Eötvös number and is given by,

$$Eo' = \frac{g \left(\rho_q - \rho_p \right) d_h^2}{\sigma} \quad (15)$$

where d_h denotes the long axis of the deformable bubble or droplet in the dispersed p-th phase.

For turbulence calculations, the k-ε model with the standard wall functions is selected. k and ε denote the turbulent kinetic energy and the dissipation rate of k, respectively. The governing equations for k and ε for the continuous q-th phase and the dispersed l-th phase are as follows:

$$
\begin{aligned}
\nabla \bullet \left(\alpha_q \rho_q \vec{U}_q k_q \right) = & \nabla \bullet \left(\alpha_q \left(\mu_q + \frac{\mu_{t,q}}{\sigma_k} \right) \nabla k_q \right) + \left(\alpha_q G_{k,q} - \alpha_q \rho_q \epsilon_q \right) \\
& + \sum_{i=1}^{N} K_{lq} \left(C_{lq} k_l - C_{ql} k_q \right) - \sum_{i=1}^{N} K_{lq} \left(\vec{U}_l - \vec{U}_q \right) \bullet \frac{\mu_{t,l}}{\alpha_l \sigma_l} \nabla \alpha_l \\
& + \sum_{i=1}^{N} K_{lq} \left(\vec{U}_l - \vec{U}_q \right) \bullet \frac{\mu_{t,q}}{\alpha_q \sigma_q} \nabla \alpha_q
\end{aligned}
\quad (16)
$$

$$
\begin{aligned}
\nabla \bullet \left(\alpha_q \rho_q \vec{U}_q \epsilon_q \right) = & \nabla \bullet \left(\alpha_q \frac{\mu_{t,q}}{\sigma_\epsilon} \nabla \epsilon_q \right) \\
& + \frac{\epsilon_q}{k_q} \left[
\begin{array}{l}
C_{1,\epsilon} \alpha_q G_{k,q} - C_{2,\epsilon} \alpha_q \rho_q \epsilon_q \\
+ C_{3,\epsilon} \left(
\begin{array}{l}
\sum_{i=1}^{N} K_{lq} \left(C_{lq} k_l - C_{ql} k_q \right) \\
- \sum_{i=1}^{N} K_{lq} \left(\vec{U}_l - \vec{U}_q \right) \bullet \frac{\mu_{t,l}}{\alpha_l \sigma_l} \nabla \alpha_l \\
+ \sum_{i=1}^{N} K_{lq} \left(\vec{U}_l - \vec{U}_q \right) \bullet \frac{\mu_{t,q}}{\alpha_q \sigma_q} \nabla \alpha_q
\end{array}
\right)
\end{array}
\right]
\end{aligned}
\quad (17)
$$

where

$$C_{lq} = 2 \quad (18)$$

and

$$C_{ql} = 2 \left(\frac{\eta_{lq}}{1 + \eta_{lp}} \right). \quad (19)$$

Here, η_{lp} is the ratio between the characteristic times of the energic turbulent eddies for the continuous q-th phase and the dispersed l-th phase, which is given by,

$$\eta_{lq} = \frac{\tau_{t,lq}}{\tau_{F,lq}}, \quad (20)$$

$$\tau_{t,lq} = \frac{\tau_{t,q}}{\sqrt{1 + C_\beta \xi^2}}, \quad (21)$$

And

$$\tau_{F,lq} = \frac{\alpha_l \rho_q}{K_{lq}} \left(\frac{\rho_l}{\rho_q} + C_v \right), \tag{22}$$

where

$$\xi = \frac{|\overrightarrow{v}_{lq}| \tau_{t,q}}{L_{t,q}} \tag{23}$$

and

$$C_\beta = 1.8 - 1.35 cos^2 \theta. \tag{24}$$

θ is the angle between the mean velocity and the mean relative velocity of the bubble or droplet for the dispersed l-th phase. $L_{t,q}$ represents the length scale of the turbulent eddies, which is defined as follows:

$$L_{t,q} = \sqrt{\frac{3}{2}} C_\mu \frac{k_q^{3/2}}{\in_q}. \tag{25}$$

In Eqs. (16) and (17), $\overrightarrow{U}_q$ is the phase-weighted velocity of the q-th phase. $\mu_{t,q}$ and $G_{k,q}$ are the turbulent viscosity and the production of the turbulent kinetic energy of the q-th phase, which results from

$$\mu_{t,q} = \rho_q C_\mu \frac{k_q^2}{\epsilon_q} \tag{26}$$

and

$$G_{k,q} = \mu_{t,q} \left(\nabla \overrightarrow{v}_q + (\nabla \overrightarrow{v}_q)^T \right) : \nabla \overrightarrow{v}_q. \tag{27}$$

C_v, $C_{1,\varepsilon}$, $C_{2,\varepsilon}$, $C_{3,\varepsilon}$, C_μ, σ_k and σ_ε are the model constants that equal to 0.5, 1.44, 1.92, 1.3, 0.09, 1.0, and 1.3, respectively.

To account for the mass, momentum and energy transfer between oil and water phases more accurately, an interfacial area concentration, χ, is used in this study with the Hibiki-Ishii model[20]. For the continuous q-th phase and the dispersed p-th phase, the equation for χ is as follows:

$$\nabla \bullet (\rho_p \overrightarrow{v}_p \chi_p) = \frac{1}{3} \frac{D\rho_p}{D_t} \chi_p + \rho_p (S_{RC} + S_{TI}) \tag{28}$$

where S_{RC} and S_{TI} are the terms for coalescence sink by random collisions and breakup due to turbulence, respectively, calculated from

$$S_{RC} = -\frac{\Gamma_C}{\psi^{11/3}} \frac{\epsilon^{1/3} \alpha_p^{1/3} \chi^{5/3}}{(\alpha_{p,max} - \alpha_p)} exp \left[-\frac{K_c \psi^{5/6} \rho_f^{1/2} \epsilon^{1/3}}{\sigma^{1/2}} \left(\frac{\alpha_p}{\chi_p} \right)^{5/6} \right] \tag{29}$$

and

$$S_{TI} = -\frac{\Gamma_B}{\psi^{11/3}} \frac{\epsilon^{1/3} (1 - \alpha_p) \chi^{5/3}}{\alpha_p^{2/3} (\alpha_{p,max} - \alpha_p)} exp \left[-\frac{K_B \sigma}{\psi^{5/3} \rho_q \epsilon^{2/3}} \left(\frac{\chi_p}{\alpha_p} \right)^{5/3} \right]. \tag{30}$$

Here, Γ_C, K_C, Γ_B, and K_B are 0.188, 0.129, 0.264, and 1.37, respectively. ψ denotes a factor for the spherical shape of the dispersed phase and corresponds to $1/36\pi$. Note that the energy equation is not solved in this study because the flow is assumed to be isothermal, and a pressure drop across the separator are insufficient to lead a significant flashing effect.

Numerical implementation

The size of the oil droplets is determined so that it corresponds to the Sauter-mean diameter of 0.1 mm to 1 mm. A constant diameter of 2 mm is assumed for the air bubbles. A coupled scheme is used to solve the conservation equations simultaneously. The spatial discretization is performed using the following schemes: Least Squares Cell Based for gradient, pressure staggering option (PRESTO!) for the pressure, second-order upwind for the momentum, quadratic upstream interpolation for convective kinematics (QUICK) for the volume fraction, and first-order upwind for the turbulent kinetic energy, turbulent dissipation rate, and interfacial area concentration. Convergence is determined not only by ensuring that the residuals of all variables fall below 10^{-3}, but also by monitoring the water volume fraction at the water and oil outlets. The solution is considered fully converged when the water volume fraction at outlets stabilized. For all cases, this occurs after approximately 14,000 iterations.
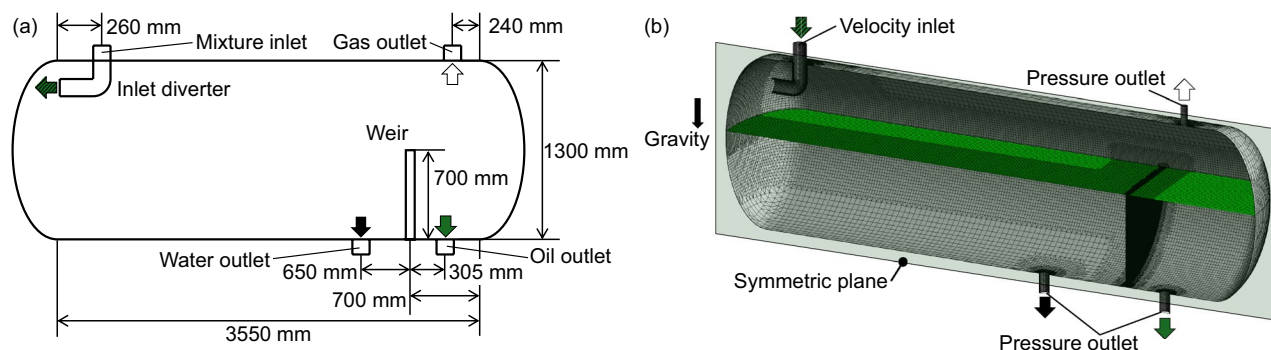
Fig. 1. Geometry of the horizontal gravity separator: (**a**) side view showing dimensions and (**b**) isometric view showing boundary conditions and grid system.

Fluid	Density [kg/m³]	Viscosity [mPa-s]	Surface tension [mN/m]
Gas	7.43	0.2	–
Oil	874.6	31.04	–
Water	903.9	1.8	–
Gas-oil	–	–	20.58
Gas–water	–	–	48.74
Oil–water	–	–	3.25

Table 1. Thermophysical properties of the working fluids.

Case	Gas inflow rate [m³/d]	Oil inflow rate [m³/d]	Water inflow rate [m³/d]	Pressure at water outlet [Pa]
Case 1	447.9	50.24	123.2	7,537.2
Case 2	447.9	50.24	123.2	7,492.8
Case 3	447.9	50.24	123.2	7,448.5
Case 4	447.9	50.24	123.2	7,421.9

Table 2. Operating conditions of the four scenarios.

Geometry and operating conditions

Figure 1a illustrates the construction of the separator examined in the present study. It has a vessel with a diameter of 1.3 m and a seam-to-seam length of 3.55 m. The inlet diverter is a reversed pipe that has the mixture inlet at a distance of 260 mm from the left seam. The water and oil outlets are located on the bottom side and 955 mm apart each other. The gas outlet is on the top side and 240 mm apart from the right seam. The weir is located between the water and oil outlets. It is 700 mm high and at 700 mm from the right seam.

Since the geometry of the separator is symmetric with respect to the vertical plane passing through the central axis of the vessel (symmetric plane), half of the separator is modeled (Fig. 1b). Velocity and pressure outlet conditions are applied to the mixture inlet and three outlets, respectively. Gravity exerts from the top side to bottom side. Figure 1b shows the grid system as well which will be described below.

Table 1 summarizes the thermophysical properties of the three working fluids. Note that the properties of gas and water phases differ from those of air and water at 1 atm and 20℃. The gas phase has a density of 7.43 kg/m³ and viscosity of 0.2 mPa-s. In addition, the density and viscosity of water are 903.9 kg/m³ and 1.8 mPa-s. The oil phase has a density of 874.6 kg/m³ and a viscosity of 31.04 mPa-s. The oil density corresponds to an API gravity of 29, which is specified as follows:

$$°API = \frac{141.5}{\gamma} - 131.5 \tag{31}$$

where γ denotes the specific gravity of the oil at 40℃. Here, API stands for American Petroleum Institute. The API gravity presents how the crude oil is heavier compared to water (API gravity of water is 10). According to the API gravity, the crude oil is distinguished as light, medium, heavy, or extra heavy oils. The oil of the present study is in the range of API gravity for medium oil ranging from 22.3 to 31.1[21].

Table 2 summarizes the four cases considered in this study. The inflow rates for the gas, oil, and water phases are constant for every case. The water outlet pressure varies from 7537.2 to 7421.9 Pa. The water outlet pressure is determined by calculating the hydrostatic pressure of the water phase at heights of 700 mm, 695 mm, 690 mm,
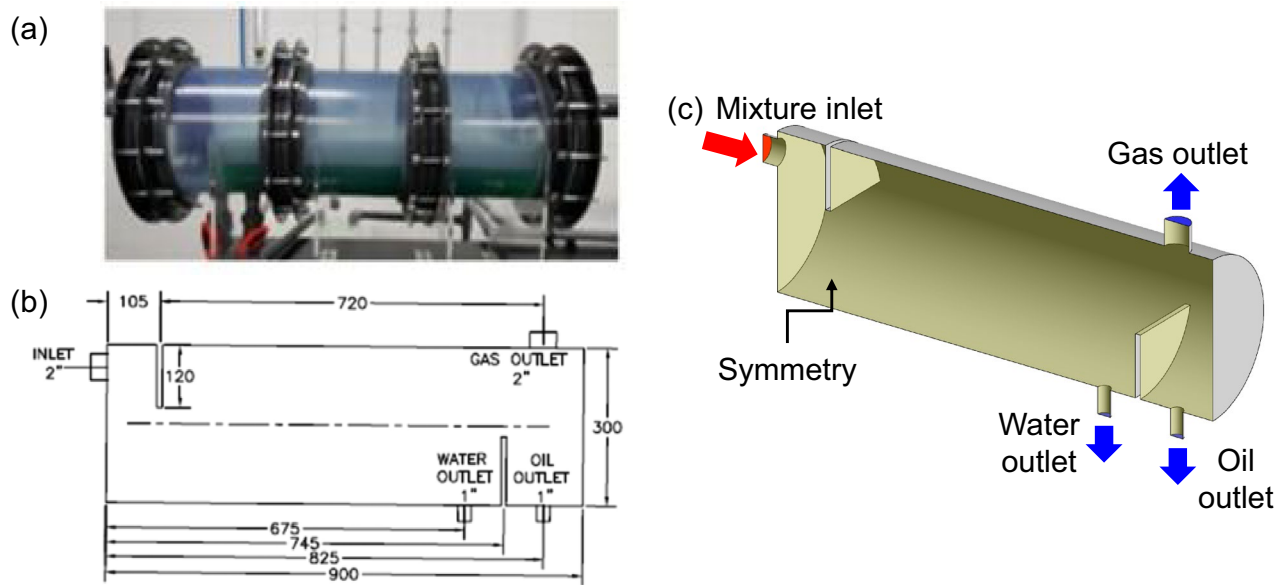
Fig. 2. (**a**) Photograph and (**b**) schematic representation of the separator by Ahmed et al.[10]. (**c**) Modeling of their separator in the present study.

Fluid	Density [kg/m³]	Viscosity [mPa-s]	Surface tension [mN/m]
Gas	1.23	1.84×10^{-2}	–
Oil	850	161.5	–
Water	1,000	1.0	–
Gas-oil	–	–	30.4
Gas–water	–	–	72.0
Oil–water	–	–	4.8

Table 3. Thermophysical properties of the working fluids of Ahmed et al.[10].

and 687 mm from the bottom of the vessel. Note that the four outlet pressure conditions in Table 2 are empirically selected to explore the sensitivity of separation performance to changes in water outlet pressure. These values are chosen to span a range in which significant variations in separation efficiency are expected. In addition, the flow rates for gas, oil, and water represent base conditions for the separator shown in Fig. 1, determined following conventional sizing methodologies[4–8].

Mesh independence test and validation

This study adopts the experimental study of Ahmed et al.[10] to test the independence of the numerical results on the grid system and to validate the numerical method. Figure 2a and b show a photograph and the design of the separator, respectively. Their separator has a vessel diameter of 300 mm and a length of 900 mm. A plate-type inlet diverter with a height of 120 mm and weir with a height of 150 mm are installed. Figure 2c shows the three-dimensional modeling for the numerical simulation with one mixture inlet and three outlets for each phase. Table 3 summarizes the thermophysical properties of the working fluids used by Ahmed et al. Notably, the viscosity of oil is 161.5 mPa-s, which is more than 160 times the viscosity of water.

For the separator proposed by Ahmed et al.[10], a mesh independence test is performed for four grid systems: coarse, medium, fine, and fine (see Fig. 3). The grids are generated using the cut-cell method that organizes a majority of grid systems with cuboid cells. Smaller cells are created both near the wall boundary and internal geometries, such as near the inlet and outlets, inlet diverter, and weir. In addition, more cells are placed where an interface between the phases is expected. As summarized in Table 4, the resulting number of cells for the coarse, medium, fine, and finer grid systems are 61,246, 209,381, 472,536, and 1,023,790, respectively. While a limited number of cells exhibit orthogonal quality below 0.15 or equivolume skewness above 0.9 in regions near the inlet diverter, the weir, and the outlet zones, the overall mesh quality is acceptable. Most cells have equivolume skewness less than 0.5 and shell squish index below 0.9, indicating good element shape and minimal distortion[16]. Table 4 also shows the water fraction at the oil outlet for four grid systems. The water fraction at the oil outlet decreases comparatively large between the medium and fine grid systems. Therefore, the fine grid system is the best choice among the four grid systems in terms of convergence of the numerical results and computational cost.
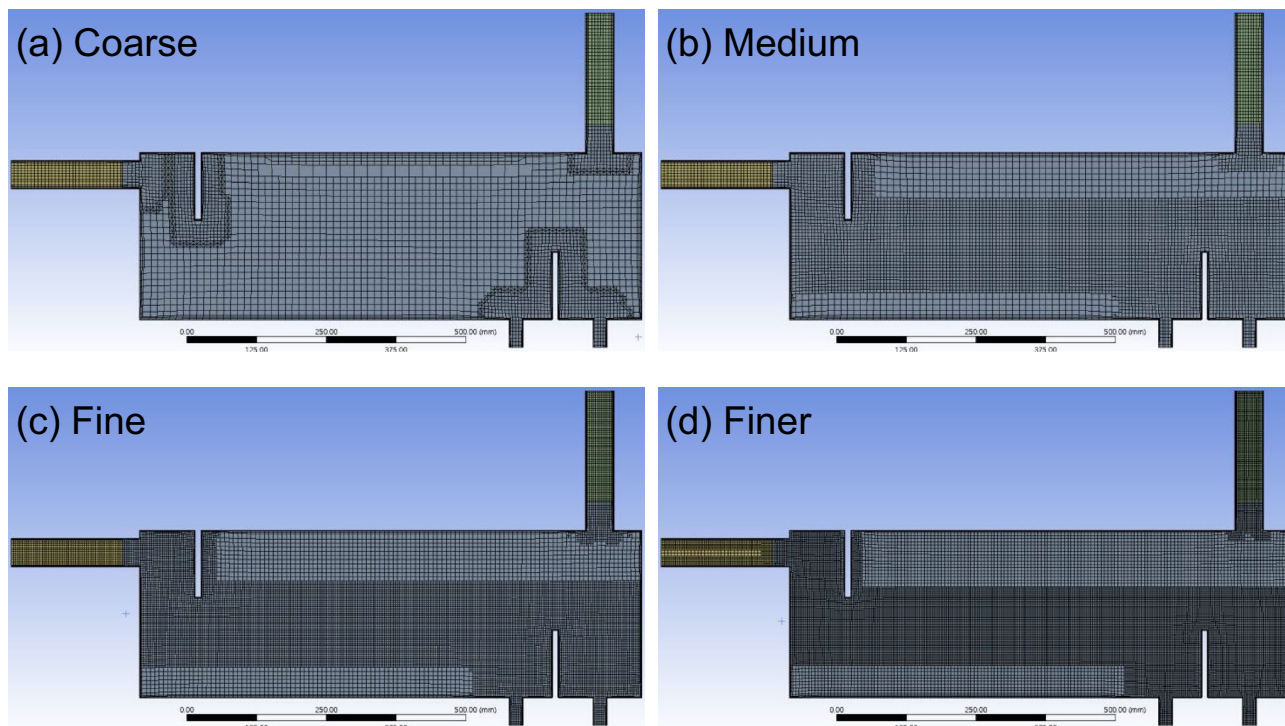
Fig. 3. Four grid systems for the mesh independence test: (**a**) coarse, (**b**) medium, (**c**) fine, and (**d**) finer.

| Grid system	Number of cells	Water fraction in oil outlet [%]
Coarse	61,246	56.43
Medium	209,381	56.39
Fine	472,536	53.85
Finer	1,023,790	52.94

Table 4. Summary of mesh independence test for four grid systems.

Case	Gas [LPM]	Oil [LPM]	Water [LPM]	Water fraction in oil outlet Present	Ahmed et al.[10]
Inflow condition 1	30	9.1	9.1	11.0%	23.5%
Inflow condition 2	30	22.7	22.7	30.0%	52.0%

Table 5. Comparison of numerical results with experimental results of Ahmed et al.[10].

To confirm the validity of the proposed numerical method, the water fraction at the oil outlet is compared with the numerical results of this study and the experimental results of Ahmed et al.[10]. Table 5 summarizes the two inflow conditions and their corresponding results. The gas inflow rates are identical under both conditions, whereas the water and oil inflow rates are different.

It is found that both the numerical and experimental results show the same tendency that the water fraction at the oil outlet increases as the inflow rates of the oil and water increase. For both cases, the water fraction at the oil outlet obtained from the numerical analysis in this study is smaller than the measured value. The difference between the numerical and the experimental results can be attributed to the setting of the outlet conditions. In the numerical analysis of this study, the same outlet conditions were set regardless of the inlet flow conditions. However, Ahmed et al.[10] controlled the water and oil levels and flow rates through the outlet valves of the separator for each experimental condition. As can be confirmed from the numerical analysis results described below, the performance of the separator can vary depending on the outlet conditions. In other words, the water fraction at the oil outlet can be similarly changed by changing the outlet boundary conditions. Therefore, the authors have judged that the present numerical method is enough to simulate the flow behavior and the performance tendency of the separator for different inflow conditions.
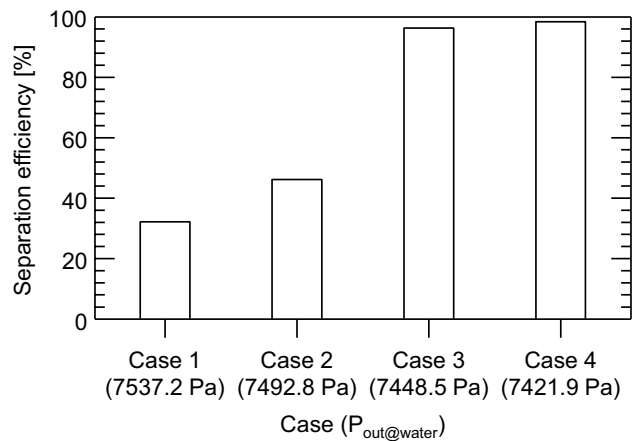
Fig. 4. Separation efficiency for the four cases with different pressures at the water outlet.
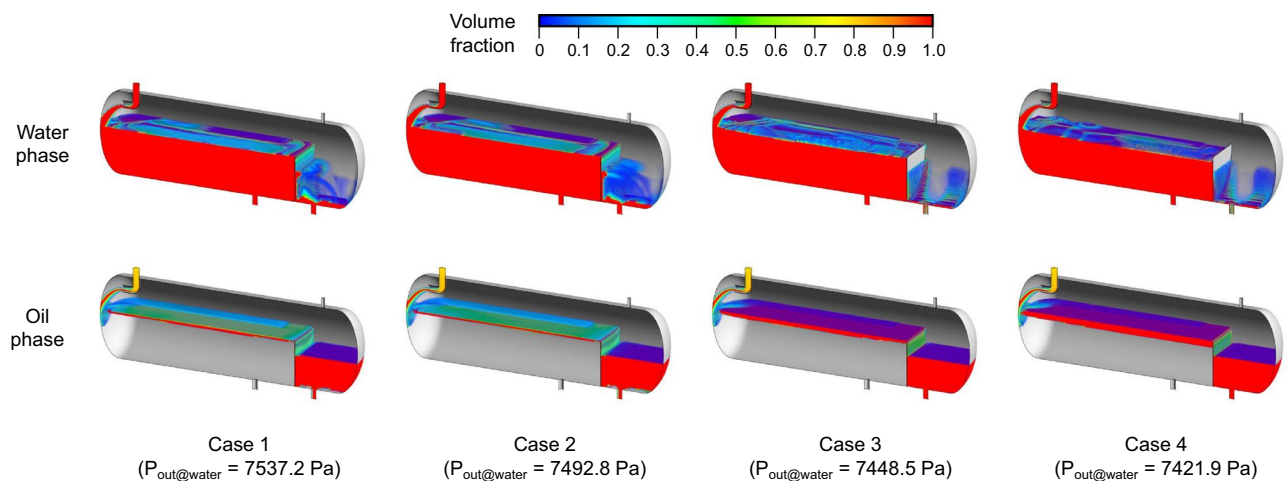
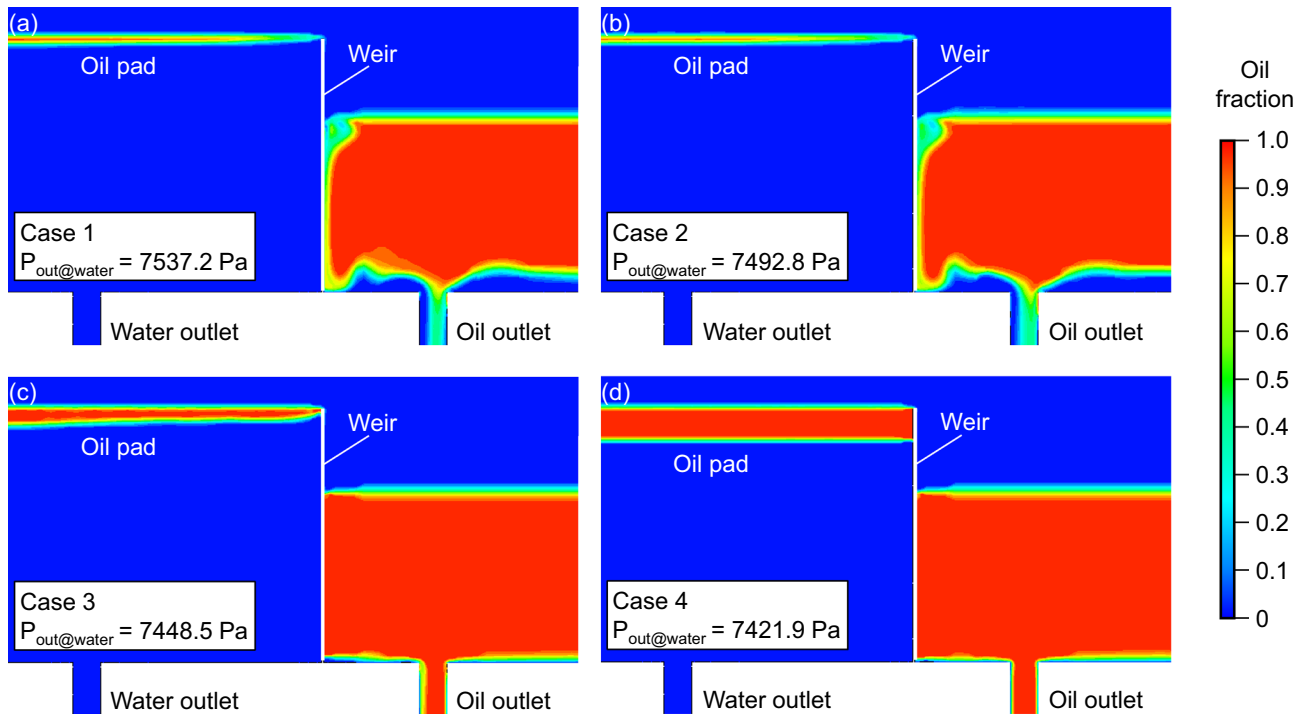**Fig. 5**. Distribution of volume fraction for water and oil phases for four cases.

Numerical results

The separation efficiency is an important indicator of the separator performance and is defined as the ratio between the water flow rate at the water outlet and the water flow rate at the inlet. Figure 4 shows the separation efficiency for four cases with different pressures at the water outlet. The separation efficiency increases when the pressure at the water outlet decreases. In particular, the separation efficiency increases sharply from 46.18% to 96.31% between Cases 2 and 3, where the pressure at the outlet decreases from 7492.8 to 7448.5 Pa. These results indicate that the pressure at the water outlet must be lower than 7492.8 Pa under the current inlet conditions for the mixture to achieve a high separation efficiency.

In this study, the flow field is investigated to determine the cause of the variations in separation efficiency. Figure 5 displays the distribution of the volume fraction of the water and oil phases in the four cases from an isometric perspective. In all cases, the majority of the water volume remains in the settling section, which is located upstream of the weir. A relatively small portion of water flows over the weir and reaches the oil outlet. However, the volume of water in Cases 1 and 2 is more in the downstream of the weir than in Cases 3 and 4. Oil phase plunging from the inlet diverter penetrates the water phase in the inlet diverter section, but rises rapidly. The oil phase begins to form an oil pad very close to the inlet diverter section. In the settling section, an oil pad is placed over the water phase. In contrast to the water phase, all oil volumes reach the oil outlet.

Figure 6 shows the oil phase distribution near the weir. The distribution is similar in Cases 1 and 2. The oil pad becomes thinner as it is closer to the weir. The oil fraction at the liquid interface near the weir is less than 0.5. However, as the pressure at the water outlet decreases in Cases 3 and 4, the thickness of the oil pad increase. In Case 3, the oil pad near the weir becomes thinner, but the oil fraction at the liquid interface near the weir is 1.0. In Case 4, the thickness of the oil pad increases further, and the thinning of the oil pad near the weir disappears.

Figure 7 shows the water phase distribution at the height of the weir, 700 mm, for the four cases from the top view. In Cases 1 and 2, the oil pad is only formed well near the symmetric plane; the water fraction increases near both the wall and the weir. In Case 3, the water fraction increases only very near the wall and is equal to

Fig. 6. Distribution of volume fraction for the water and oil phases for (**a**) case 1, (**b**) case 2, (**c**) case 3, and (**d**) case 4.
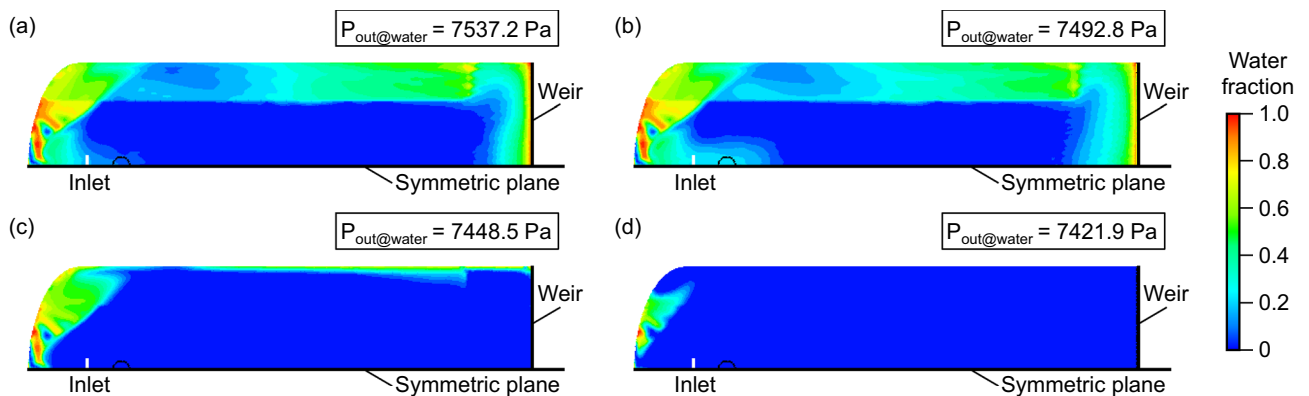

Fig. 7. Distribution of water fraction at the height of weir for (**a**) case 1, (**b**) case 2, (**c**) case 3, and (**d**) case 4.

zero near the weir. In Case 4, the water fraction is 0 even near the wall. The thinning of the oil pad near the wall is attributed to the uneven shear stress at the liquid interface.

The velocity difference between the gas and liquid phases induces shear stress at the interface. However, owing to the non-slip condition of the wall, the velocity gradient increases with increasing distance from the center. This results in higher shear stress at the interface near the wall and hinders the formation of the oil pad. However, the oil pad in Case 4 is sufficiently thick to nullify the effect of the shear stress. The size of the inlet diverter sections for the four cases are also identified in Fig. 7. As the pressure at the water outlet decreases and the oil pad thickens, the region affected by the plunge in the inflow mixture decreases.

The horizontal distribution of the oil pad is related to the velocity field in the liquid phase. Figure 8 shows the velocity vectors in the vertical planes at distances of 0, 1.4, and 2.8 m from the upstream seam for the four cases. At a distance of 0 m, a large counterclockwise circulation is formed in all cases owing to the momentum of the plunging inflow and the curved end of the separator. As the flow moves downstream, the circulation weakens and almost disappears at 1.4 m. Up to a distance of 1.4 m the difference between the cases is small. However, at a distance of 2.8 m, which is just before the weir, the velocity vector field shows a difference between the cases. In Cases 1 and 2, an upward flow is observed near the liquid interface, and a downward flow occurs simultaneously.
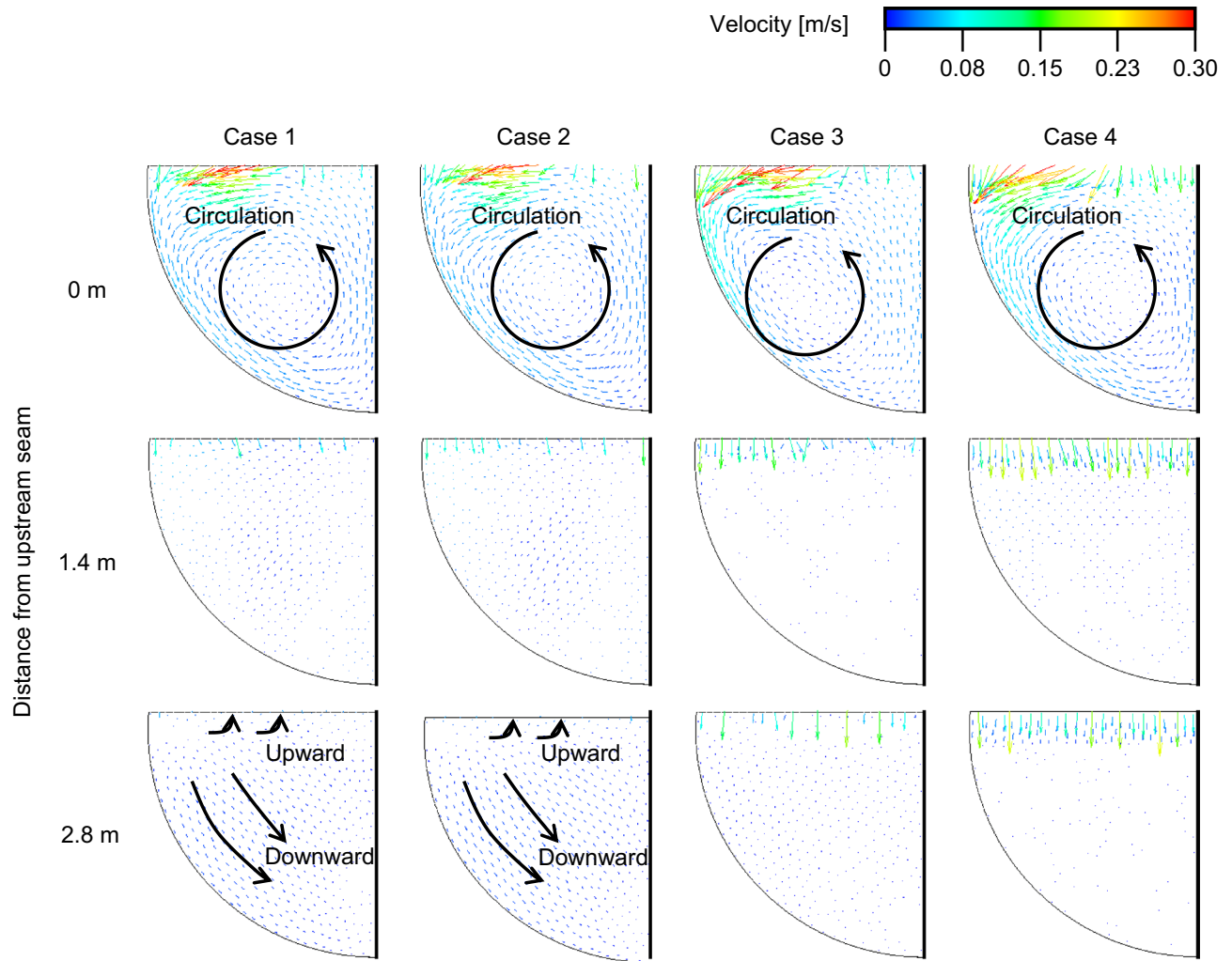
Fig. 8. Velocity vector fields in vertical planes at distances of 0, 1.4, and 2.8 m from the upstream seam for four cases.

In Case 3, the velocity magnitude decreases and upward flow is rarely observed. In Case 4, the velocity of the liquid phase is almost zero.

As shown in Fig. 8, the downward velocity at the liquid interface increases with a decrease in the pressure at the water outlet, that is, an increase in the thickness of the oil pad. This is attributed to the viscosity of oil, which is 17 times greater than that of water.

Figure 9 shows the distribution of the oil fraction along the vertical line on the symmetrical plane near the upstream side of the weir. As aforementioned, the thickness of the oil pad increases with decreasing pressure at the water outlet. The hydrostatic pressure can be compared with the numerical results, as the pressure at the water outlet influences the thickness of the oil pad. Assuming that the water and oil phases are well separated just above the water outlet and the gas–liquid interface is at the height of weir, the water height can be derived as follows:

$$h_{water,pred} = \left(\frac{P_{out@water}}{g} - \rho_o H_{weir} \right) (\rho_w - \rho_o)^{-1} \tag{32}$$

where ρ_w and ρ_o denote the densities of the water and oil phases, respectively. H_{weir} is the height of the weir, 700 mm. The prediction of the water height using Eq. (32) is indicated as a dotted horizontal line in Fig. 9. In Case 1, the prediction shows good agreement with the numerical result. However, the predicted values of Eq. (32) deteriorate when the pressure at the water outlet decreases. This discrepancy suggests the nonlinearity of multiphase phenomena in the separator and the importance of experimental and numerical studies.

The oil pad thickness influences the residence time of water and oil phases. The residence time is a time that a fluid takes while flows from the inlet to the outlet of the separator. Typically, the separation performance increases with increasing the residence time. Mean residence time (MRT) is a measure of the residence time for each phase. MRT can be obtained from[22]
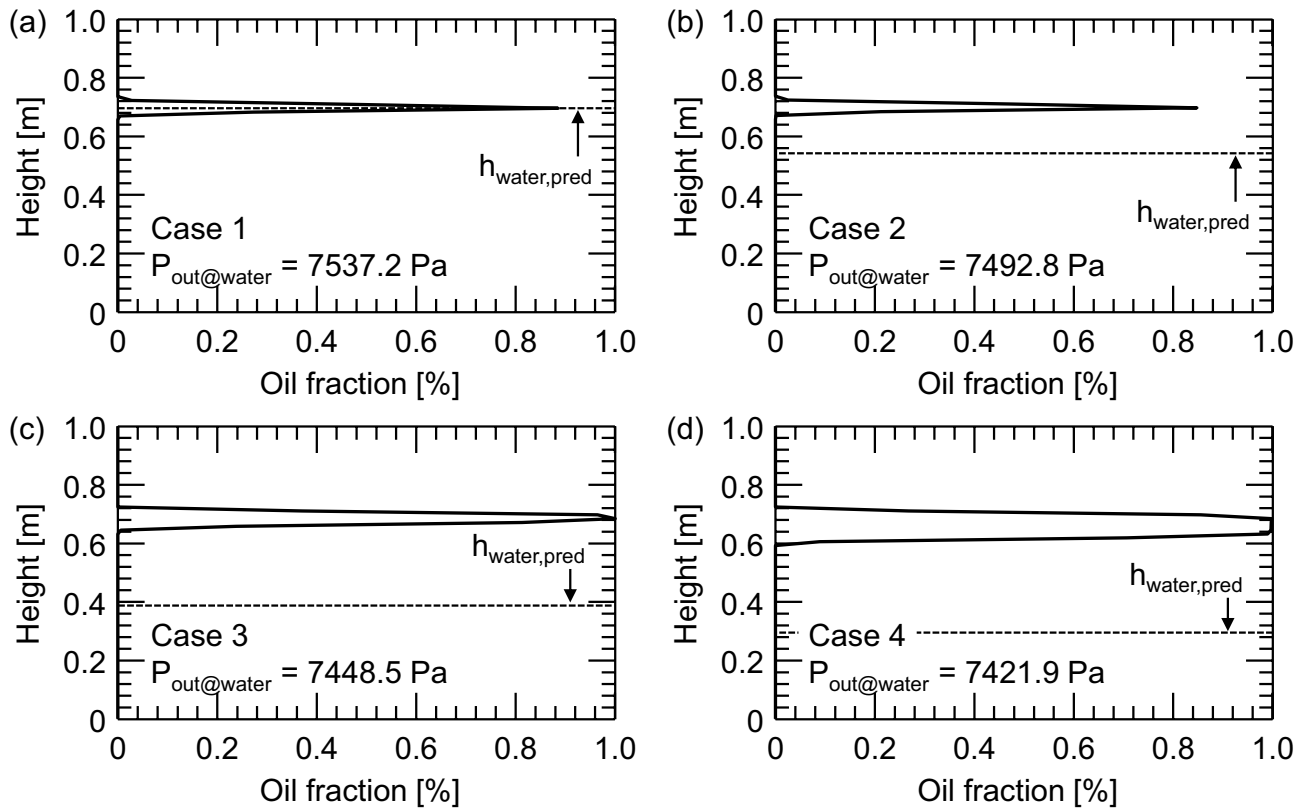
Fig. 9. Oil phase fraction by height for water outlet pressures of (**a**) 7537.2 Pa, (**b**) 7492.8 Pa, (**c**) 7448.5 Pa and (**d**) 7421.9 Pa, showing the prediction of the height of the water interface.
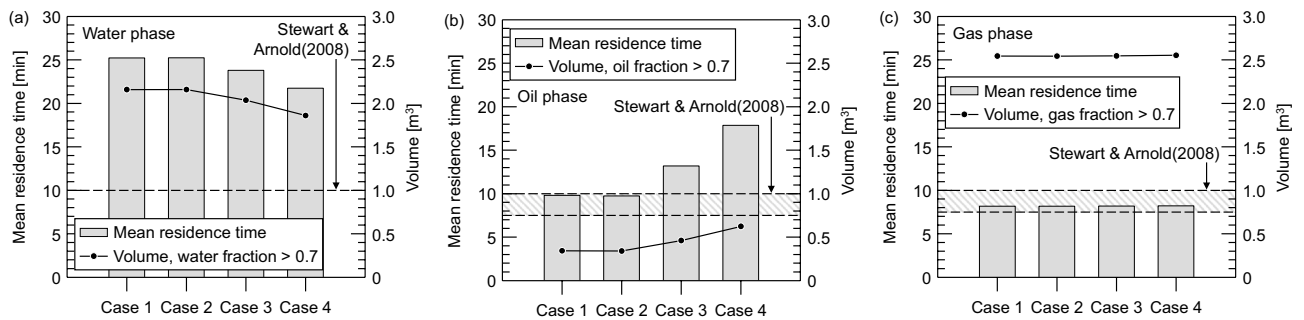
Fig. 10. Mean residence time and volume with associated phase fraction larger than 0.7 for (**a**) water phase, (**b**) oil phase, and (**c**) gas phase.

$$\mathrm{MRT} = \frac{V_q}{Q_q} \tag{33}$$

where V_q and Q_q denote the volume occupied by the q-th phase and inlet flow rate of q-th phase, respectively. Note that this study obtains V_q by summing up the local volumes of corresponding fluid that exceeds 0.7.

Figure 10 shows the MRTs of water, oil, and gas phases for four cases. In Figs. 10a and b, the MRT of water and oil phases merely changes between Cases 1 and 2. However, it changes noticeably for Cases 3 and 4; as the pressure at the water outlet decreases, the MRT decreases for the water phase and increases for the oil phase. The foregoing is due to the thickening of oil pad which results in the increase of oil phase volume and the decrease in the water phase volume, as already shown above. Meanwhile, in Fig. 10c, the MRT and volume for the gas phase is rarely affected by the pressure at the water outlet for all cases.

Figure 10 also compares the MRT obtained from the current simulations and the design criteria for MRT suggested by Stewart and Arnold[8]. They recommended the residence time at least 7.5 to 10 min for the oil with a 20–30 API gravity. In addition, they suggested a residence time of 10 min for the water phase when

the laboratory or field data is unavailable. As shown in Fig. 10, the present separator is expected to satisfy the residence time criteria of Stewart and Arnold. The water and oil phases stay more than 20 min and 9 min, respectively. However, the high separation efficiency is obtained only for Cases 3 and 4. The foregoing suggests that the enough thickness of oil pad is essential for a good separation performance along with the high residence time.

Conclusions

In this study, the influence of outlet pressure at the water outlet on the performance of a horizontal gravity separator was investigated. The numerical method was validated by comparing the numerical results with experimental data. The performance of the separator was varied for four selected pressures at the water outlet. A lower outlet pressure resulted in a higher separation efficiency. In particular, when the water outlet pressure decreases from 7492.8 Pa to 7448.5 Pa, the separation efficiency increases rapidly. The formation of an oil pad was also discussed for different water outlet pressures. Owing to the unevenly distributed interfacial shear stress, the thickness of the oil pad decreases near the sidewall. The velocity field associated with the formation of the oil pad was also discussed. The water height resulting from the hydrostatic pressure equation was compared with the numerical results. In most cases, a large discrepancy was found. Lastly, the mean residence time of water, oil, and gas phases was discussed for four conditions of water outlet pressures and was compared with the existing design criteria on the residence time. This comparison suggested the oil pad thickness needs to be considered for a high separation performance along with the residence time. In conclusion, the water outlet pressure should be kept below 7448.5 Pa for the oil phase to have sufficient thickness of the oil pad to ensure efficient separation. It should be noted that the observed trend is based on fixed inlet flow rates, thermophysical properties, geometries, and constant dispersed phase properties such as bubble diameter. In practice, such parameters may vary with operating conditions and design. Therefore, the authors plan future studies to fully understand the effects of pressure at all three outlets of the separator on separation efficiency under different conditions by varying those parameters that can affect the results. Based on the extensive results, the authors will construct the non-dimensional and generalized correlations for predicting the separation efficiency and suggesting the threshold of the optimum operating condition.

Data availability

The datasets used and/or analysed during the current study available from the corresponding author on reasonable request.

References

1. Zou, C. *Unconventional petroleum geology* (2nd ed.) 36–40 (Elsevier, 2017).
2. Gouxin, L. et al. Progress, challenges and prospects of un-conventional oil and gas development of CNPC. *China Petrol. Explor.* **27**, 1–11 (2022).
3. Qiu, Z., Zhou, L., Bai, L., El-Emam, M. A. & Agarwal, R. Empirical and numerical advancements in gas-liquid separation technology: A review. *Geoenergy Sci. Eng.* **233**, 212577 (2024).
4. Monnery, W. D. & Svrcek, W. Y. Successfully specify three-phase separators. *Chem. Eng. Prog.* **90**, 29–40 (1994).
5. Bothamley, M. & Campbell, J. M. Gas/liquid separators: Quantifying separation performance-part 1. *Oil and Gas Facilities* **2**, 21–29 (2013).
6. Bothamley, M. & Campbell, J. M. Gas/liquid separators: Quantifying separation performance-part 2. *Oil and Gas Facilities* **2**, 35–47 (2013).
7. Bothamley, M. & Campbell, J. M. Gas/liquid separators: Quantifying separation performance-part 3. *Oil and Gas Facilities* **2**, 34–47 (2013).
8. Stewart, M. & Arnold, K. *Gas-liquid and liquid-liquid separators* 65–174 (Gulf Professional, 2008).
9. Ahmed, T., Russell, P. A., Hamad, F. & Gooneratne, S. Experimental analysis and computational-fluid-dynamics modeling of pilot-scale three-phase separators. *SPE Prod. Oper.* **34**, 805–819 (2019).
10. Ahmed, T. G., Russell, P. A., Makwashi, N., Hamad, F. & Gooneratne, S. The effects of inlet flow rates and slenderness ratio on the separation performance of a horizontal three-phase separator. *SPE Prod. Oper.* **36**, 962–975 (2021).
11. Pun, K. et al. Experimental investigation of the parameters that affect droplet size and distribution for design calculations of two-phase separators. *Heliyon* **9**, e15397 (2023).
12. Pun, K., Hamad, F., Pun, M., Lawson, G. & Russell, P. Experimental investigation of the effect of slenderness ratio and retention time on the separation performance of a two-phase horizontal separator. *Chem. Eng. Res. Des.* **207**, 221–231 (2024).
13. Carvalho, A. J. G., Galindo, D. C., Tenório, M. S. C. & Marinho, J. L. G. Modeling and simulation of a horizontal three-phase separator: Influence of inlet flow. *Braz. J. Petrol. Gas* **14**, 137–155 (2020).
14. Carvalho, A. J. G., Galindo, D. C., Tenório, M. S. C. & Marinho, J. L. G. Modeling and simulation of a horizontal three-phase separator: Influence of physicochemical properties of oil. *Braz. J. Petrol. Gas* **14**, 205–220 (2021).
15. Baghi, M. D. Y. & Karimi, M. Investigating the mean residence time in a two-phase oil-water separator using volume of fluid multiphase theory in computational fluid dynamics simulation. *SPE Prod. Oper.* **38**, 527–536 (2023).
16. ANSYS Inc., ANSYS & Fluent, T. Guide, release 19.1 (2019).
17. Takamasa, T. & Tomiyama, A. Three-dimensional gas-liquid two-phase bubbly flow in a C-shaped tube in *Proc. of Ninth International Topical Meeting on Nuclear Reactor Thermal Hydraulics (NURETH-9)*, San Francisco, CA, USA 3–8 (1999).
18. Tomiyama, A. Struggle with computational bubble dynamics. *Multiphase Sci. Technol.* **10**, 369–405 (1998).
19. Frank, T., Shi, J. M. & Burns, A. D. Validation of Eulerian multiphase flow models for nuclear safety applications in *Proc. of Third International Symposium on Two-Phase Flow Modeling and Experimentation*, Pisa, Italy 22–25 (2004).
20. Hibiki, T. & Ishii, M. One-group interfacial area transport of bubbly flows in vertical round tubes. *Int. J. Heat Mass Transf.* **43**, 2711–2726 (2000).
21. Correa Pabón, R. E. & Souza Filho, C. R. Crude oil spectral signatures and empirical models to derive API gravity. *Fuel* **237**, 1119–1131 (2019).

22. Kharoua, N. L., Khezzar, H. & Saadawi, H. CFD modelling of a horizontal three-phase separator: A population balance approach. *Am. J. Fluid Dyn.* **3**, 101–118 (2013).

Author contributions
Hong-Cheol Shin contributed to the conceptualization, formal analysis, data processing, validation, original draft preparation, and the revised manuscript. Hyeonseok Seo and Hee-La Jang contributed to investigation and critically revised the manuscript to enhance its quality. Inju Hwang secured the funding and supervised the overall research and project progression. All authors reviewed and approved the final version of the manuscript.

Declarations

Competing interests
The authors declare no competing interests.

Additional information
Correspondence and requests for materials should be addressed to H.S.

Reprints and permissions information is available at www.nature.com/reprints.

Publisher's note Springer Nature remains neutral with regard to jurisdictional claims in published maps and institutional affiliations.